Predictive Control With Battery Power Sharing Scheme for Dual Open-End-Winding Induction Motor Based Four-Wheel Drive Electric Vehicle

Utkal Ranjan Muduli, *Member, IEEE*, Abdul R. Beig, *Senior Member, IEEE*, Ranjan Kumar Behera, *Senior Member, IEEE*, Khaled Al Jaafari, *Senior Member, IEEE*, and Jamal Y. Alsawalhi, *Member, IEEE*

***Abstract*—For high-power electric vehicles (EVs), the drive propulsion based on induction motors is emerging as economical alternative. Compared to conventional induction motors, the open-end winding induction motor (OEWIM) requires only half the dc-bus voltage for the given torque. The EV power train based on the dual two-level voltage-source inverter (VSI)-fed OEWIM with isolated dc sources is used in this research. For uniform state-of-charge (SoC) distribution, the power flow from each isolated source needs to be controlled. A two-stage model-predictive direct torque control (MPDTC) scheme is proposed to balance the SoC of batteries by proper selection of the VSI voltage vectors. The proposed MPDTC scheme is free from weighting factor tuning and uses a ranking method to predict the optimal voltage vectors. The superiority of the proposed controller in terms of battery SoC balancing is demonstrated. The performance of the proposed MPDTC EV drive is verified for the FTP75 and HFET driving cycles under different operating conditions, both by simulation and hardware experimental tests.**

***Index Terms*—Battery state-of-charge (SoC) control, electric vehicle (EV) propulsion systems, model-predictive direct torque control (MPDTC), open-end winding induction motor (OEWIM), vehicle power train control.**

Manuscript received September 18, 2020; revised December 22, 2020, March 29, 2021, and May 27, 2021; accepted June 15, 2021. Date of publication June 29, 2021; date of current version February 1, 2022. This work was supported in part by the Abu Dhabi Education and Knowledge under Grant AARE18-102 and in part by the Khalifa University Advanced Power and Energy Center under Grant RC2-2018/21-06. *(Corresponding author: Utkal Ranjan Muduli.)*

Utkal Ranjan Muduli is with the Khalifa University of Science and Technology, Abu Dhabi 127788, UAE, He was with the Department of Electrical Engineering, Indian Institute of Technology Patna, Patna 801103, India (e-mail: utkal.muduli@ku.ac.ae).

Abdul R. Beig, Khaled Al Jaafari, and Jamal Y. Alsawalhi are with the Advanced Power and Energy Center, Department of Electrical Engineering and Computer Science, Khalifa University of Science and Technology, Abu Dhabi 127788, UAE (e-mail: balanthi.beig@ku.ac.ae; khaled.aljaafari@ku.ac.ae; jamal.alsawalhi@ku.ac.ae).

Ranjan Kumar Behera is with the Department of Electrical Engineering, Indian Institute of Technology Patna, Patna 801103, India (e-mail: rkb@iitp.ac.in).

Color versions of one or more figures in this article are available at https://doi.org/10.1109/TIE.2021.3091919.

Digital Object Identifier 10.1109/TIE.2021.3091919

I. Introduction

ELECTRIC transportation is needed for a sustainable future, as it gives better control and management of pollution. The need to reduce CO_2 emission, especially in urban areas, is forcing governments to bring regulations, which promote the use of electric vehicles (EVs) and electric transportation in public transportation service [1]–[3]. In the present scenario, small individually owned electric cars and bikes have only 5% utilization, so it is important to build suitable high-power vehicle power trains for large cars, buses, cargo trucks, aircraft, ships, etc. It is estimated that the EVs will replace one-third of the total road vehicles by 2030. Most of the present-day small cars use permanent magnet synchronous motors (PMSMs) as prime movers. Rare-earth magnetic materials used in PMSMs have limited availability and expensive. Developing drive trains based on alternative motors that do not rely on permanent magnets, such as induction motors (IMs), is an emerging research trend in EVs. IMs are widely used in industry with a wide range of control methods available in the literature [4]–[6]. However, IMs have low power density and lower efficiency compared to PMSMs. Hence, extensive research study in the field of IMs is a crucial factor in improving its power density and drive range [4], [6].

From the safety point of view, low battery voltages (in the range 24–96 V) are preferred for EVs. However, at these voltage levels, the size of the IM increases as thick conductors are required to carry higher currents. IMs with higher voltages (say in the range 100–400 V) are better for heavy EVs, and the corresponding dc-bus voltage for inverters needs to be in the range of 200–800 V. Higher dc-bus voltages can be achieved either by connecting the batteries in series or by using suitable high-gain dc–dc converters. The series connection of batteries reduces the reliability and also increases the size, cost, and weight of the battery bank. The latter approach requires multiple stages of dc–dc conversion leading to increased losses and size, as the existing dc–dc converters have low gain (less than 3). Also, with multiple stages, regeneration will be complex and inefficient. This problem can be addressed by using open-end winding induction motors (OEWIMs). Compared to the conventional IM drive, the OEWIM drive develops same torque for half the dc-bus voltages [7], [8]. Additionally, the dual two-level voltage-source inverter (VSI)-fed OEWIM drive has improved

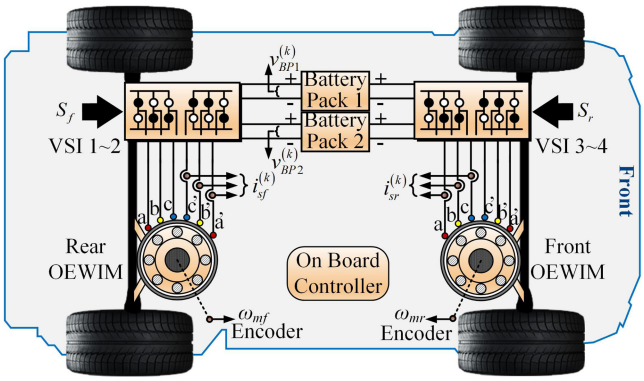

Fig. 1. Dual-OEWIM-based D4WD topology for EV.

voltage waveform and harmonic profile similar to the three-level VSI-fed drive [9]. Unlike conventional IM drives, the OEWIM drive is powered by two independent dc buses, which are advantageous due to distributed battery configuration and also higher reliability due to built-in fault-tolerant operation (FTO). Various power train mechanisms such as front-wheel drive (FWD), rear-wheel drive (RWD), four-wheel drive (4WD), and all-wheel drive (AWD) are adopted in road EVs [6], [10]–[15]. Although FWD and RWD both are economical, they lack FTO. In 4WD and AWD, in-wheel drives are controlled separately, which results in high-performance drive but needs complicated control action during failure mode. In the differential 4WD (D4WD), differentials are adopted between the front and rear axle, and between the wheels, which ensures safe and stable turning as well as forward acceleration. Also, in the event of any one motor failure, the D4WD can be run as FWD or RWD accordingly. So, in this article, the EV with D4WD based on two OEWIM drives is considered [16], and the corresponding drive arrangement is shown in Fig. 1.

The variations in OEWIM electrical parameters, such as resistance and inductance, cause significant variations in torque and speed response. These torque and speed variations affect the performance of the EV during running. Direct torque control (DTC) is suitable in EV applications because of the rapid and accurate torque response and avoids uncertainties over parameter variation. In addition, DTC has less computational complexity than other control techniques and does not need variables to be decoupled and matrix transformation [10], [16]–[18]. The DTC-based OEWIM D4WD for EV with dual isolated battery packs (BPs) is given in [16]. In addition to normal operation, this drive train has some attractive features such as lower dc-bus voltage and ability to generate full torque when one of the inverters powering the front OEWIM (FM) and rear OEWIM (RM) fails. However, one limitation of this drive train is that the loading of these BPs may differ due to variations in environmental conditions, manufacturing tolerances, aging, charging characteristics, internal resistance, and misalignment of charging levels [19]. The weaker BP may get loaded more and, therefore, discharged faster, thus creating load imbalance and performance degradation. Both BPs require proportional power sharing and even discharging at the same voltage level to achieve excellent driving performance. This article addresses these issues and improves the performance of the drive given in [16].

Recently, several digital-signal-processor- and field-programmable-gate-array-based high-performance controllers such as model-predictive control (MPC) are becoming an option to meet the high-speed optimized computational requirements [20]. The MPC can predict the IM drive performance few steps ahead (i.e., number of steps decided by computational resource) and can select the most suitable voltage vector (VV) to achieve good torque performance and low torque ripple. This can be achieved by choosing a lower sampling rate for the controller and thereby reducing the switching frequency. The MPC-based EV power trains given in [20]–[22] focus on drive control by incorporating long- or short-horizon look ahead of driving conditions [20] and stochastic MPC with a detailed evaluation of the driver model based on the Markov chain by forecasting the maximum power demand for the shortest prediction horizon [23]. In [21], the stochastic MPC for parallel hybrid EV power-split control is proposed to reduce relative fuel consumption, where MPC is validated by applying the Markov chain model with a future road-grade estimate. The MPC-based control is used in [22] to reduce the probabilistic future energy consumption. This article incorporates the efficiency of both MPC and DTC, thereby developing an improved model-predictive DTC (MPDTC) scheme. For MPDTC operation, offline/online tuning of the weight factor is a significant concern for the EV application. The solution of the weighting factor selection problem is indicated by the algebraic criterion in [24]. In [25], sequential MPDTC without the weight factor is provided with different cost functions for torque and flux. The MPC method without weight factor tuning is also suggested in [7] with ranking analysis, but the influence of varied operating conditions leads to less robustness. The MPDTC scheme in [26] solves the problem due to weight factor tuning and parameter variation at the cost of increased computational complexity. However, the methods of [7] and [26] cannot be used to balance the state of charge (SoC) of BPs while considering the dual-motor D4WD EV. The proposed MPDTC is used for the future estimation of rotational speed and torque and thus the total power demand for the prediction horizon. At the same time, the battery SoC balance is achieved by optimizing the proposed MPDTC objective function with a proper study of the active power sharing control scheme for the dual-OEWIM-powered D4WD EV. This is a substantial improvement over [16] with improved drive performance. The novelty and main contributions of this article are as follows.

1) Seamless torque and speed distribution between FM and RM drives are achieved by analyzing active power sharing between the VSI and BPs.
2) An improved MPDTC algorithm is proposed for the OEWIM-based D4WD EV, where the torque and flux control objectives are integrated with the battery SoC balancing.
3) The proposed MPDTC scheme achieves high-performance dynamic speed and torque response

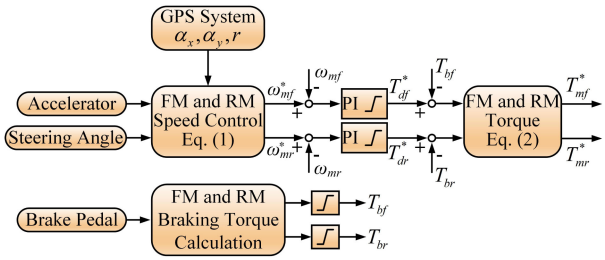

Fig. 2. Speed control and torque reference calculation unit.

with reduced stator current harmonics at lower switching losses.

4) The EV performance was validated both by simulation and experiments at various operating conditions such as acceleration, deceleration, and turning for FTP75 and HFET driving cycles.

The rest of this article is organized as follows. A brief description of the dual-OEWIM D4WD and the proposed MPDTC with SoC control is given in Section II. The implications of simulation and experimental findings are described in Section III. Finally, Section IV concludes this article.

II. Proposed MPDTC Controller With SoC Balancing for D4WD

A dual-OEWIM-based D4WD with two isolated BPs is shown in Fig. 1. The EV propulsion system is used to supply power to both FM and RM with four conventional two-level voltage-source inverters (2L-VSI). Battery pack-1 (BP1) supplies power to VSI1 and VSI4 of the FM drive, while battery pack-2 (BP2) supplies power to VSI2 and VSI3 of the RM drive. The dc-bus voltages of both BP1 and BP2 are kept equal, i.e., $V_{\mathrm{BP1}} = V_{\mathrm{BP2}} = V_{\mathrm{dc}}/2$.

A. Speed and Torque Distribution

The functional block diagram of speed control and torque reference calculation is shown in Fig. 2. The reference speed of the FM (ω^*_{mf}) and the steering angle (δ) are set either manually (through the acceleration pedal, the brake pedal, and the steering) or automatically (using GPS data) [16]. The reference speed (ω^*_{mr}) of RM is computed from ω^*_{mf} using

$$\omega^*_{mr} = \omega^*_{mf} \cos\delta. \tag{1}$$

The actual speeds of FM (ω_{mf}) and RM (ω_{mr}) are sensed using speed encoders and used as feedback for the speed controller, as shown in Fig. 2. The speed error signals corresponding to FM and RM are controlled by adopting two separate proportional–integral (PI) controllers that generate reference driving torque for FM (T^*_{df}) and RM (T^*_{dr}), respectively. T_{bl} ($l \in \{f, r\}$) represents the gross torque developed by the EV during regenerative braking. Let T^* be the total reference torque required to drive the vehicle. It is dependent on the various force factors acting on the vehicle, including total mass of the vehicle [16]. Based on the exerted longitudinal forces on the front and rear wheels of the dual-OEWIM D4WD EV, the corresponding torque is developed by FM and RM, respectively. Hence, the optimal

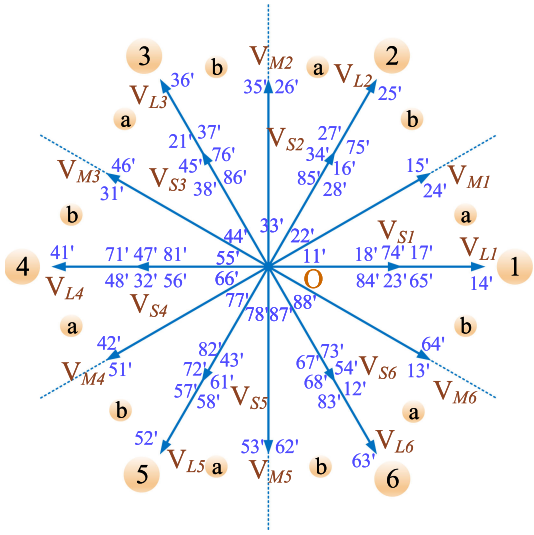

Fig. 3. Possible VVs for the dual-VSI-fed OEWIM drive.

torque distribution for both FM (T^*_{mf}) and RM (T^*_{mr}) can be found by solving the unconstrained nonlinear optimization problem, where the objective function can be expressed as in (2). The torque distribution factor "W" is considered as the optimization variable and can be evaluated by using (3)

$$\begin{aligned} T^*_{mf} &= \min\left\{(T^*_{df} - T_{bf}), (R_w F_{xf})\right\} = WT^* \\ T^*_{mr} &= \min\left\{(T^*_{dr} - T_{br}), (R_w F_{xr})\right\} = (1-W)\,T^* \end{aligned} \tag{2}$$

$$W = T^*_{mf} / \left(T^*_{mf} + T^*_{mr}\right) \tag{3}$$

where F_{xf} and F_{xr} are the longitudinal forces required by front-end and rear-end differential, respectively [16].

B. Dual-VSI Model With Possible Switching States

Let k represents the kth (present) sample with a sampling time of T_s. The switching states of the each leg of the dual 2L-VSI, in Fig. 1, namely, $S^{(k)}_{al}$, $S^{(k)}_{bl}$, $S^{(k)}_{cl}$, $S^{(k)}_{a'l}$, $S^{(k)}_{b'l}$, and $S^{(k)}_{c'l}$, can be operated at either "1" or "0" states. The kth sample of phase voltages can be synthesized from the measured dc-link voltages ($V^{(k)}_{\mathrm{BP1}}$ and $V^{(k)}_{\mathrm{BP2}}$) using these internal generated switching states as in (4), thus reducing the number of voltage sensors to two

$$\begin{bmatrix} v^{(k)}_{aa'l} \\ v^{(k)}_{bb'l} \\ v^{(k)}_{cc'l} \end{bmatrix} = \begin{bmatrix} S^{(k)}_{al} \\ S^{(k)}_{bl} \\ S^{(k)}_{cl} \end{bmatrix} V^{(k)}_{\mathrm{BP1}} - \begin{bmatrix} S^{(k)}_{a'l} \\ S^{(k)}_{b'l} \\ S^{(k)}_{c'l} \end{bmatrix} V^{(k)}_{\mathrm{BP2}}, \quad l \in \{f, r\}. \tag{4}$$

The possible switching states for the dual-2L-VSI-fed OEWIM drive are 64 (2^6), as shown in Fig. 3. The VVs corresponding to these switching states are categorized as large (6), medium (12), small (36), and zero (10) vectors. The proper use of redundancies in small and medium vectors can result in switching loss reduction, FTO, and SoC balancing. Out of 36 small VVs, 24 small VVs can be used along with four zero VVs (78′, 88′, 87′, and 77′), when an inverter connected to the OEWIM fails. Remaining 12 small VVs are used during normal operation of the OEWIM. In total, 34 VVs (large: 6, medium:

12, small: 12, and zero: 4) are useful for the operation of the proposed MPDTC-based OEWIM drive.

C. One-Step Delay-Compensated OEWIM Model

The OEWIM model is analyzed in a two-phase power-invariant $\alpha\beta$ (stationary) reference frame as

$$X_{sl}^{(k)} = \sqrt{\frac{2}{3}} \sum_{\substack{m=1 \\ l\in\{f,r\}}}^{3} X_{ph,l}^{(k)} e^{j\frac{2\pi(m-1)}{3}} \tag{5}$$

where X is a generic variable representing a space vector corresponding to voltage (v) or current (i) or flux (ψ) variables and $ph \in \{aa,'\ bb,'\ cc'\}$ represent the active phases of both FM and RM. The term m represents the number of phases and superscript k represents the present sample. The flux estimation model of the OEWIM is defined as

$$\begin{bmatrix} \psi_{sl}^{(k)} \\ \psi_{rl}^{(k)} \end{bmatrix} = \left(I + A^{(k-1)}T_s\right) \begin{bmatrix} \psi_{sl}^{(k-1)} \\ \psi_{rl}^{(k-1)} \end{bmatrix} + T_s \begin{bmatrix} v_{sl}^{(k-1)} \\ 0 \end{bmatrix} \tag{6}$$

$$A^{(k-1)} = \begin{bmatrix} -\dfrac{1}{\sigma\tau_s} & \dfrac{k_r}{\sigma\tau_s} \\ \dfrac{k_s}{\sigma\tau_r} & -\dfrac{1}{\sigma\tau_r} + j\omega_{rl}^{(k-1)} \end{bmatrix}$$

where the backward Euler approximation (i.e., $d\psi/dt = (\psi^{(k)} - \psi^{(k-1)})/Ts$) is used to define the dynamics of the motor. The cogging torque, magnetic saturation, hysteresis, and eddy current losses are neglected for this simplified OEWIM model.

The state-space discrete-time model of the OEWIM is stated in (6)–(10). The response of the closed-loop control drive can be improved by using delay compensation to account for the delay associated with feedback sensors. Hence, a one-step delay is introduced by using the forward Euler approximation (i.e., $d\psi/dt = (\psi^{(k+1)} - \psi^{(k)})/Ts$) at a sampling interval T_s[27]. The stator flux information at the $(k+1)$th state is obtained using the kth state of stator flux and voltage information. In addition, the predicted current at the $(k+1)$th state in (8) can be achieved from the $(k+1)$th state stator flux information. The speed dynamic relation for both FM and RM is presented in (10)

$$\begin{bmatrix} \psi_{sl}^{(k+1)} \\ \psi_{rl}^{(k+1)} \end{bmatrix} = \left(I + A^{(k)}T_s\right) \begin{bmatrix} \psi_{sl}^{(k)} \\ \psi_{rl}^{(k)} \end{bmatrix} + T_s \begin{bmatrix} v_{sl}^{(k)} \\ 0 \end{bmatrix} \tag{7}$$

$$\begin{bmatrix} i_{sl}^{(k+1)} \\ i_{rl}^{(k+1)} \end{bmatrix} = C \begin{bmatrix} \psi_{sl}^{(k+1)} & \\ & \psi_{rl}^{(k+1)} \end{bmatrix} \tag{8}$$

$$T_{ml}^{(k+1)} = \Im\left(p\bar{\psi}_{sl}^{(k+1)} i_{sl}^{(k+1)}\right) \tag{9}$$

$$\omega_{rl}^{(k+1)} = \omega_{rl}^{(k)} + \frac{pT_s}{J}\left(T_{ml}^{(k)} - T_{Ll}^{(k)}\right)$$

$$A^{(k)} = \begin{bmatrix} -\dfrac{1}{\sigma\tau_s} & \dfrac{k_r}{\sigma\tau_s} \\ \dfrac{k_s}{\sigma\tau_r} & -\dfrac{1}{\sigma\tau_r} + j\omega_{rl}^{(k)} \end{bmatrix}, \quad C = \begin{bmatrix} \dfrac{1}{\sigma L_s} & -\dfrac{k_r}{\sigma L_s} \\ -\dfrac{k_s}{\sigma L_r} & \dfrac{1}{\sigma L_r} \end{bmatrix} \tag{10}$$

where I represents the 2×2 complex identity matrix with j as the complex operator. $T_{ml}^{(k+1)}$ is the electromagnetic torque developed by FM and RM. $\sigma = 1 - L_m^2/L_sL_r$ is the magnetizing coefficient, $\tau_s = L_s/R_s$ and $\tau_r = L_r/R_r$ are the stator and rotor time constants, respectively, $k_s = L_m/L_s$ and $k_r = L_m/L_r$ are the stator and rotor constants, respectively, p is the number of pole pairs, $\omega_{rl}^{(k)}$ is the rotor electrical speed of FM and RM at the kth instant, and the subscript l represents f: front and r: rear.

D. Power Distribution Analysis

The EV system is designed for the optimum use of battery power over its full operating range; hence, the analysis of the power flow plays an important role. The EV can achieve its highest speed when the torque developed in the OEWIMs is at its maximum level. Thus, the maximum power requirement of the EV is determined by the product of the highest speed and the maximum developed torque. The rating of the OEWIMs in the D4WD is decided on the basis of this maximum power demand, irrespective of the available BP energy. Under steady-state condition, the power input to the stator of both FM (P_{sf}) and RM (P_{sr}) is expressed as

$$P_{sl} = \underbrace{R_{sl}\left[(i_{sl}^{\alpha})^2 + \left(i_{sl}^{\beta}\right)^2\right]}_{\text{Copper loss}} + \underbrace{\frac{\omega_{rl}}{p_l}T_{ml}}_{\text{Shaft power}}, \quad l \in \{f,\ r\}. \tag{11}$$

According to (11), the distribution of the speed and torque, as decided by (1) and (2), determines how the total power of the shaft is shared. The power flow from the two BPs can be regulated by tuning the distribution factor W. For example, a total current demand I^* of the EV is distributed among the four VSIs as $i_1 \ldots i_4$, respectively, as their input currents. Now, the current demand for FM (i_{FM}) and RM (i_{RM}) can be expressed as

$$i_{\text{FM}} = i_1 + i_2 = WI^*, \quad i_{\text{RM}} = i_3 + i_4 = (1 - W)\, I^*. \tag{12}$$

When the EV accelerates, the RM experiences more load than FM, and thus, W $(0 < W < 0.5)$ is tuned to a smaller value to meet higher current demand of the RM. While EV is in the deceleration mode, FM experiences more load than RM and W $(0.5 < W < 1)$ is tuned to a higher value to meet higher current demand of the FM. In accordance with (2), the magnitude of the W is adjusted based on the distribution of the longitudinal forces on the EV wheels. For power sharing among BPs, the SoCs of both BPs need to be estimated by the Coulomb counting method as follows [28]:

$$\text{SoC}_n = \text{SoC}_n^{(0)} - \frac{1}{C_n}\int i_n dt, \quad n \in \{\text{BP1}, \text{BP2}\} \tag{13}$$

where $\text{SoC}_n^{(0)}$, C_n, and i_n represent initial SoC concentrations, capacity of BPs, and current drawn from the BPs, respectively. Due to the presence of internal impedance of BPs, there is a possibility of battery voltage fluctuations during EV operation. This results in the difference in SoC concentration of both BPs, and thus, unequal currents are drawn from BPs. Unequal currents further aggravate the SoC imbalance. Hence, for SoC balancing

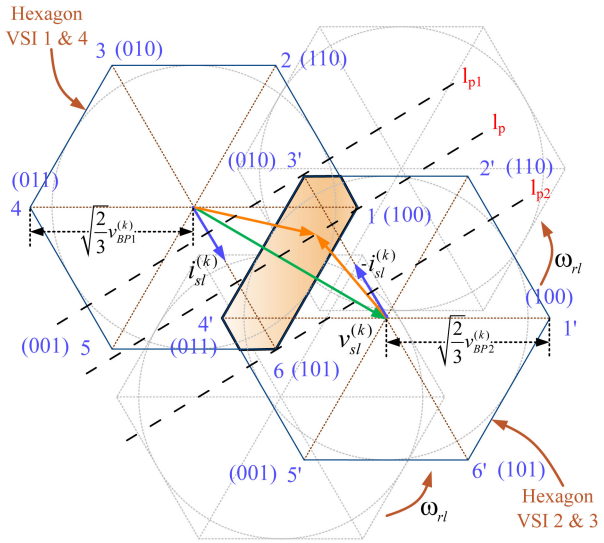

Fig. 4. Power sharing between the inverters connected to FM and RM.

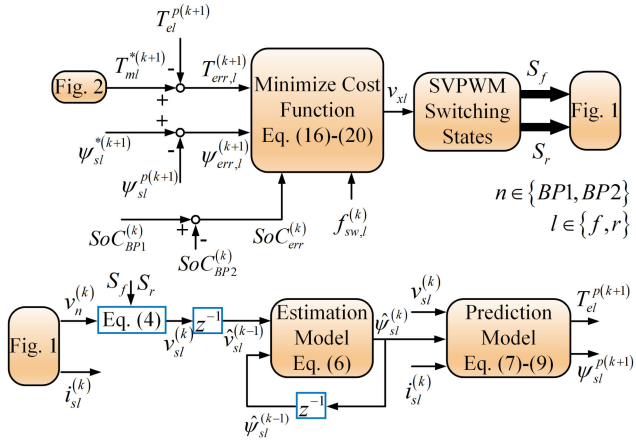

Fig. 5. Proposed MPDTC controller with SoC balancing for dual-OEWIM-based D4WD EV.

in a time interval T_s, a proper switching vector selection from the redundant VVs is necessary.

Fig. 4 shows the schematic diagram of the VV distribution of individual inverters connected to either FM/RM in the $\alpha\beta$ frame and illustrates power sharing between them. The green vector indicates the resultant stator VV ($v_{sl}^{(k)}$) of both FM and RM ($l \in \{f : \text{FM}, r : \text{RM}\}$). $v_{sl}^{(k)}$ can be calculated using the relations given in (4), (5), and (14). $v_{sf}^{(k)}$ ($v_{sr}^{(k)}$) is the difference of $v_{s1}^{(k)}$ and $v_{s2}^{(k)}$ ($v_{s4}^{(k)}$ and $v_{s3}^{(k)}$) by considering unequal voltage level of BPs, i.e., $V_{\text{BP1}}^{(k)}$ and $V_{\text{BP2}}^{(k)}$

$$v_{sf}^{(k)} = v_{s1}^{(k)} - v_{s2}^{(k)} \quad \text{and} \quad v_{sr}^{(k)} = v_{s4}^{(k)} - v_{s3}^{(k)}. \tag{14}$$

For convenience, hexagon for VSI1 and VSI4 (VSI2 and VSI3) is indexed as Hex1 (Hex2). The intersection of Hex1 and Hex2 represents the shaded region and allocates the feasible linear modulation range of VSI1 and VSI2 (VSI3 and VSI4) for the essence of the VV distribution. To understand the VV representation, Hex1 is considered stationary, and the shaded hexagons are representing rotation of Hex2 around Hex1 with rotor angular speed of ω_{rl} in the $\alpha\beta$ frame. The orange vectors with magnitude of $\sqrt{\frac{2}{3}}v_{\text{BP1}}^{(k)}$ and $\sqrt{\frac{2}{3}}v_{\text{BP2}}^{(k)}$ are used to represent $v_{s1}^{(k)}$ and $v_{s2}^{(k)}$ ($v_{s4}^{(k)}$ and $v_{s3}^{(k)}$) in the shaded region, respectively. The stator current vector observed from VSI2 (VSI3) has an opposite direction to that observed from VSI1 (VSI4) and is represented by blue vectors. Hence, the output power of VSI1–VSI4 can be obtained from the voltage and current vectors as

$$\begin{aligned} P_{\text{VSI1}}^{(k)} &= \Re\left(v_{s1f}^{(k)} i_{sf}^{(k)}\right) \quad \text{and} \quad P_{\text{VSI2}}^{(k)} = -\Re\left(v_{s2f}^{(k)} i_{sf}^{(k)}\right) \\ P_{\text{VSI4}}^{(k)} &= \Re\left(v_{s1r}^{(k)} i_{sr}^{(k)}\right) \quad \text{and} \quad P_{\text{VSI3}}^{(k)} = -\Re\left(v_{s2r}^{(k)} i_{sr}^{(k)}\right). \end{aligned} \tag{15}$$

Consider that l_P is the perpendicular line to the direction of $i_{sl}^{(k)}$ and passes through the intersection of $v_{s1}^{(k)}$ and $v_{s2}^{(k)}$ ($v_{s4}^{(k)}$ and $v_{s3}^{(k)}$). l_p shows the locus of the power shared by VSI1 (VSI4) and VSI2 (VSI3) on FM (RM) operation. The locus l_{p1} indicates the minimum power shared by VSI1 (VSI4) and maximum power shared by VSI2 (VSI3). Similarly, the locus l_{p2} indicates the maximum power shared by VSI1 (VSI4) and minimum power shared by VSI2 (VSI3). Once line l_P moves beyond the range between l_{P1} and l_{P2}, it will have no intersections with the feasible region of the VV distribution; thus, the power sharing cannot be determined by l_{P1} and l_{P2}. The modified MPDTC scheme proposed in the following subsection deals with these issues, and the current sharing by two BPs can be made nearly equal (i.e., $i_1 + i_4 \approx i_2 + i_3$).

E. SoC Balancing Through the Proposed MPDTC

In conventional MPDTC, the selection of the optimal vector is based on the cost function associated with torque and flux control objectives; thus, the SoC of the BPs in the OEWIM D4WD cannot be maintained at same level. In this article, the SoC balancing of the BPs is achieved by integrating objective corresponding to SoC error in addition to the torque and flux control objectives, as shown in Fig. 5. The proposed MPDTC has several advantages over the conventional MPC[7] as listed in the following.

1) It enables a combined torque and flux control with SoC balancing in a single-objective function.
2) It eliminates the burden of weight factor tuning through optimal VV selection.
3) It mitigates the torque ripple along with stator current harmonics.
4) It evaluates the optimized VV as per the rank analysis and thus reduces the computational burden and complexities.

The cost function associated with the modified MPDTC with SoC balancing and switching frequency control is described in

$$\begin{aligned} g_l^{(k+1)} = & \underbrace{\lambda_T \left(g_{T,l}^{(k+1)}\right)^2 + \lambda_\psi \left(g_{\psi,l}^{(k+1)}\right)^2}_{\text{Conventional MPDTC}} \\ & + \underbrace{\lambda_{\text{SoC}} \left(g_{\text{SoC}}^{(k)}\right)^2}_{\text{SoC Control}} + \underbrace{\lambda_{\text{sw}} \left(g_{\text{sw},l}^{(k)}\right)^2}_{\text{Switching Loss Control}} \end{aligned} \tag{16}$$

where $g_{T,l}^{(k+1)}$, $g_{\psi,l}^{(k+1)}$, $g_{\text{SoC}}^{(k)}$, and $g_{\text{sw},l}^{(k)}$ are the control objectives obtained from multiobjective separation and is defined as

$$g_{T,l}^{(k+1)} = \left|\frac{T_{\text{err},l}^{(k+1)}}{T_N}\right| \quad \text{and} \quad g_{\psi,l}^{(k+1)} = \left|\frac{\psi_{\text{err},l}^{(k+1)}}{\psi_N}\right|$$
$$g_{\text{SoC}}^{(k)} = \left|\frac{\text{SoC}_{\text{err}}^{(k)}}{\text{SoC}_N}\right| \quad \text{and} \quad g_{\text{sw},l}^{(k)} = \left|\frac{f_{\text{sw},l}^{(k)}}{V_N}\right| \tag{17}$$

where $T_{\text{err},l}^{(k+1)} = T_{ml}^{*(k+1)} - T_{el}^{p(k+1)}$ is the torque error, $\psi_{\text{err},l}^{(k+1)} = \psi_{sl}^{*(k+1)} - \psi_{sl}^{p(k+1)}$ is the flux error, $\text{SoC}_e^{(k)} = \text{SoC}_1^{(k)} - \text{SoC}_2^{(k)}$ is the SoC error, and $f_{\text{sw},l}^{(k)} = V_{sl}^{(k-1)} - V_{sl}^{(k)}$ is the switching function error. T_N, ψ_N, and V_N are the nominal values of motor torque, stator flux, and stator voltage, respectively, for both FM and RM. SoC_N is the nominal SoC value, i.e., 100%. The weight factors (λ_T, λ_ψ, λ_{SoC}, and λ_{sw}) are set to 0.25 for eliminating the shortcomings of online/offline tuning. Hence, the value of the cost function $g_l^{(k+1)}$ is obtained within the limit [0, 1], which directly uses the present VV ($v_{sl}^{(k)}$). Implementing these objective functions with one-step prediction is difficult. Therefore, a two-step prediction is required using future VV ($v_{sl}^{(k+1)}$) to compensate the controller's delay issue, as in

$$g_{T,l}^{(k+2)} = \left|\frac{T_{\text{err},l}^{(k+2)}}{T_N}\right| \quad \text{and} \quad g_{\psi,l}^{(k+2)} = \left|\frac{\psi_{err,l}^{(k+2)}}{\psi_N}\right|$$
$$g_{\text{SoC}}^{(k+1)} = \left|\frac{\text{SoC}_{\text{err}}^{(k+1)}}{\text{SoC}_N}\right| \quad \text{and} \quad g_{\text{sw},l}^{(k+1)} = \left|\frac{f_{\text{sw},l}^{(k+1)}}{V_N}\right|. \tag{18}$$

The cost function associated with the modified MPDTC in (16) can be interpreted as (19) by implementing two-step prediction control objectives from (18):

$$g_l^{(k+2)} = \lambda_T\left(g_{T,l}^{(k+2)}\right)^2 + \lambda_\psi\left(g_{\psi,l}^{(k+2)}\right)^2 + \lambda_{\text{SoC}}\left(g_{\text{SoC}}^{(k+1)}\right)^2 + \lambda_{\text{sw}}\left(g_{\text{sw},l}^{(k+1)}\right)^2. \tag{19}$$

The key benefit of the proposed MPDTC controller is to reduce the computational burden with better drive performance. The potential benefits of the proposed method are evaluated in the two-stage selection process to optimize the VV selection and reduce computational burden. The first step is to evaluate the cost function $g_l^{(k+2)}$ with the present optimized VV instead of evaluating for all 64 available VVs, as shown in Fig. 3. The evaluated $g_l^{(k+2)}$ value is quantified within the limit [0, 1]. The available VVs are categorized into four groups (large, medium, small, and zero) with different magnitude as mentioned earlier in Section II-B. As different VV groups have different effect on torque and flux, further categorization of $g_l^{(k+2)}$ is necessary. The generated cost function in (19) is subdivided into four groups as in (20) to produce cost function index $g_{x,l}^{(k+2)}$

$$g_{x,l}^{(k+2)} = \begin{cases} +3, & \text{if } g_l^{(k+2)} \geq 0.7 \\ +2, & \text{if } 0.7 \geq g_l^{(k+2)} \geq 0.6 \\ +1, & \text{if } 0.6 \geq g_l^{(k+2)} \geq 0.3 \\ 0, & \text{if } 0.3 \geq g_l^{(k+2)} \geq 0 \end{cases} \quad l \in \{f, r\}. \tag{20}$$

The VV group selection is explained as follows.

1) The large VV group is selected for the faster torque and flux response corresponding to $g_{x,l}^{(k+2)} = +3$.
2) The medium VV group is selected on $g_{x,l}^{(k+2)} = +2$. The selected medium redundant VVs are used to maintain the SoC of the dual BPs.
3) In order to minimize the torque and flux ripple, the small VV group is selected on $g_{x,l}^{(k+2)} = +1$. As the small VV group contains more redundant VVs, it also helps to balance the SoC of dual BPs.
4) The zero vector groups are selected, while no change in torque is required, i.e., at $g_{x,l}^{(k+2)} = 0$.

The second stage involves selection of optimal VV based on the rank analysis to improve torque and flux performance along with SoC control. Here, the control objectives given in (18) are evaluated for all the available VVs in the selected VV group. As four control objectives are considered here, each VV in the selected VV group is associated with four different ranks (i.e., R_1, R_2, R_3, and R_4). The maximum number of rank values associated with each control objectives depends on the available VVs in the selected VV group. As the maximum number of VVs given in each VV group decreased to "12" for the fault-free operation of the EV, the total computational burden is minimized to 1/5 times to that of the MPC method in [7]. By selecting a small or medium VV group, a maximum of 12 ranks are required for each control objective to estimate the optimum selection of VVs. Similarly, the calculation of ranks corresponding to six VVs is required on selection of a large VV group, which further reduces the computational burden to 1/10 times to that of MPC[7]. Finally, the optimum rank (R) value is computed by minimizing the average ranking value for each VV as in (21). The VV having a minimum mean rank is known to be the optimum VV (v_{xl}) for the next sample interval T_s

$$R = \min\left(\frac{1}{4}\sum_{n=1}^{4} R_n\right). \tag{21}$$

The optimum VV v_{xl} further selects the switching pulse to operate dual VSI connected to FM and RM. For example, large VV $V_{L2}(25')$ is resulted from vector $V_2(110) - V_5'(001)$ of individual two-level switching states, as shown in Fig. 4. Switching patterns required to drive VSI stacks are further established using carrier-based space vector pulsewidth modulation (SVPWM) technique, in order to maintain the constant switching frequency. This switching strategy enhances the use of optimum VV and eliminates significant voltage harmonic with reduced switching losses. A complete block diagram of SVPWM operation is provided in Fig. 6 with the following details.

Step 1: The optimal VV (v_{xl}) generated from the two-stage MPDTC scheme goes through the axis transformation with the stator flux angle ($\angle\psi_{sl}^{p(k+1)}$) to obtain the reference VV v_{xl}^* using the relation $v_{xl}^* = v_{xl}\angle\psi_{sl}^{p(k+1)}$, i.e., $v_{xl}^* = v_{xl}e^{\angle\psi_{sl}^{p(k+1)}} = |v_{xl}^*|\angle v_{xl}^*$. Such implementation is accomplished in order to

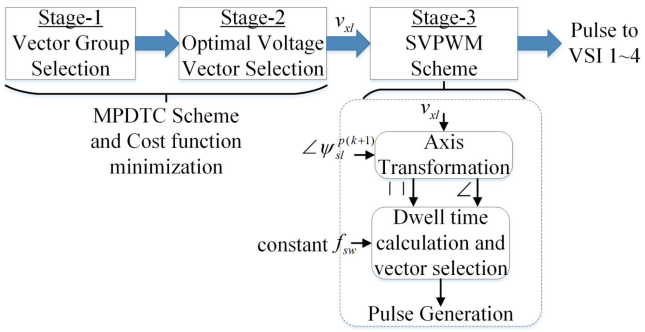

Fig. 6. Optimal VV selection and SVPWM implementation.

rotate v_{xl} in the direction of the stator flux angle in the $\alpha\beta$ plane.

Step 2: The dwell times are calculated using volt–second balancing techniques [29]. Dwell times utilizes the magnitude ($|v_{xl}^*|$) and angle ($\angle v_{xl}^*$) of v_{xl}^* for each of the sectors corresponding to the FM/RM drives.

Step 3: A carrier of user-defined switching frequency ($f_{\rm sw}$) is utilized to construct SVPWM. Using the calculated dwell times, seven timing intervals are defined for the complete switching period ($T_{\rm sw} = 1/f_{\rm sw}$). To maintain only one state transition (either 0 to 1 or 1 to 0) during all the seven timing intervals of $T_{\rm sw}$, a proper selection of switching vectors are configured as per [29]. In first half of $T_{\rm sw}$, the switching sequence starts with the zero vector followed by two adjacent active vectors and ends with the redundant/zero vector. In the next half of $T_{\rm sw}$, the switching sequence starts with the redundant/zero vector and utilizes the reflection of the VVs of the previous half. During sector changeover of v_{xl}^*, the starting vector is known; thus, new active vectors with one switching transition are selected to generate new sequence. This process of switching sequence design maintains the constant switching frequency of the drive operation. The exactness of achieving constant switching frequency can be evaluated from the state diagram of the switching sequences of each switch, which is elaborately provided in [29].

III. Results and Discussion

To evaluate the performance of the proposed MPDTC with SoC control of BPs, simulation and experimental investigations are carried out for the dual-OEWIM-based D4WD EV. The parameters of the EV model, OEWIMs, and VSIs are given in Table I. Simulation and experimental validation are carried out for an urban (FTP75) [30] and highway (HFET) driving cycles.

A. Simulation Results

Figs. 7 and 8 show the performance of the proposed drive for FTP75 and HFET driving cycles, respectively. In Figs. 7 and 8, the SoC balance is enabled at $t = t_1$ s. It is observed that

TABLE I
Simulation Parameters of the Dual-Motor D4WD EV

EV Parameters and Values
m =1847 kg, h_{cg} = 46.98 cm, R_w = 50.8 cm
l_f =152.64 cm, l_r = 135.36 cm, l = 288 cm, b = 170 cm
OEWIM Simulation Parameters
3Φ, 415 V, 35 kW, 72 A, 60 Hz, 1740 rpm, 0.87 PF
R_s =0.9529 Ω, R_r =1.133 Ω, $L_{ls} = L_{lr}$ = 5.1 mH
l_m =386.7 mH, J = 0.06 kgm^2, B = 0.001
Control Parameters
Speed controller: k_p=1.53, k_i=3.56
MPDTC controller: $\lambda_T = \lambda_\psi = \lambda_{SoC} = \lambda_{sw}$=0.25
T_N = 95 Nm, ψ_N = 0.687 wb, V_N = 415 V, SoC_N=100%

the proposed MPDTC controller is able to detect the initial SoC differences of two BPs and maintain the SoC level for $t \geq t_1$ s. The driving cycle in the above results consists of different driving conditions such as acceleration, running, turning, and deceleration. In order to observe the performance of the proposed drive, the simulation results for each driving condition are shown in Figs. 9–12. For all modes of operation, the conventional MPC[7] is applied initially from time $t = 0$ to t_1 s, while the proposed MPDTC is applied at time $t = t_1$ s. The proposed controller maintains the SoC level of BPs at $t \geq t_2$ s, and there is no SoC balance during the interval $0 \leq t < t_2$ s. Controller takes $t = t_2 - t_1$s time to achieve SoC balance.

1) During Acceleration: In Fig. 9, at the time of starting, the SoCs of BP1 and BP2 are held at 95% and 94%, respectively. Although enabling SoC balancing at t_1 s, the SoCs of BP1 and BP2 are not immediately balanced. As a consequence, the controller action takes place in such a way that more current has been taken from BP1 and less current from BP2 to balance the SoC at $t = t_2$ s. For $t \geq t_2$ s, the proposed controller maintains SoC balance of two BPs.

2) During Running: Fig. 10 evaluates the EV performance during normal road driving. Before the proposed controller enables SoC balance at $t = t_1$ s, the BP1 and BP2 SoCs are observed at 95% and 94%, respectively. Immediately after controller action, more current is taken from BP1 than BP2 to align the SoC at $t = t_2$ s. After t_2 s, the proposed controller maintains the two-BP SoC level.

3) During Turning: The EV performance is tested during a left and right turn when driving on a normal road, as shown in Fig. 11. During the turn, it is found that the RM speed is less than the FM speed and is a function of the steering angle. The proposed control is tested for SoC balance at time $t = t_1$ s while turning right. By allowing more current from BP1 than BP2, the proposed controller regulates the SoC of two BPs at $t = t_2$ s; at the same time, the satisfactory torque performance is also accomplished.

4) During Deceleration: EV is decelerated through regenerative braking, and results are given in Fig. 12. During the regenerative braking cycle, the controller enables BPs to be recharged rather than discharged. In this scenario, BP1 and BP2 SoCs are measured at 91% and 90.4%, respectively, at time $t = t_1$ s, i.e., in the vicinity of allowing SoC control. The

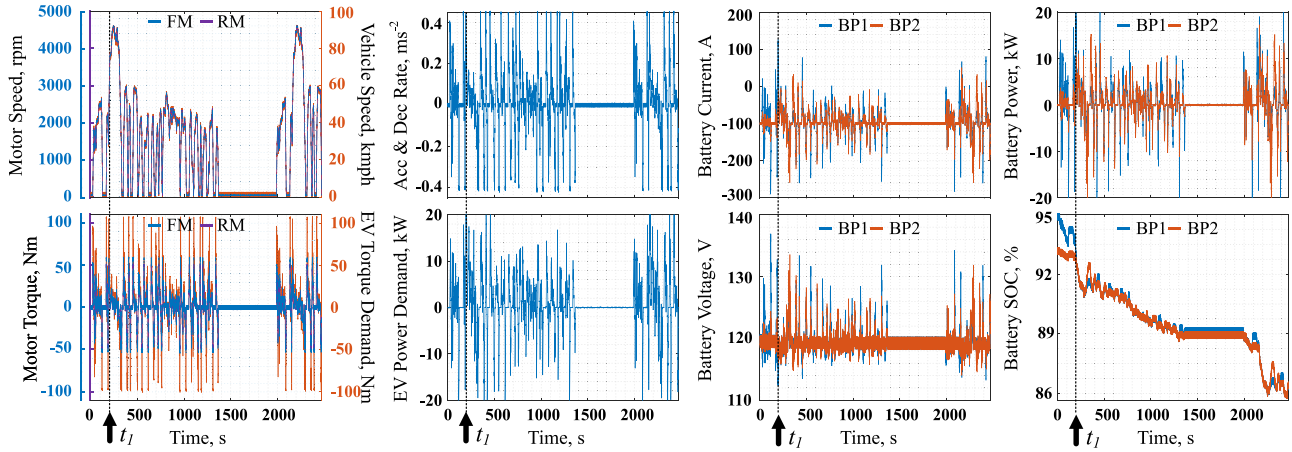

Fig. 7. Simulation results of dual motor D4WD EV with SoC balancing for FTP75 driving cycle.

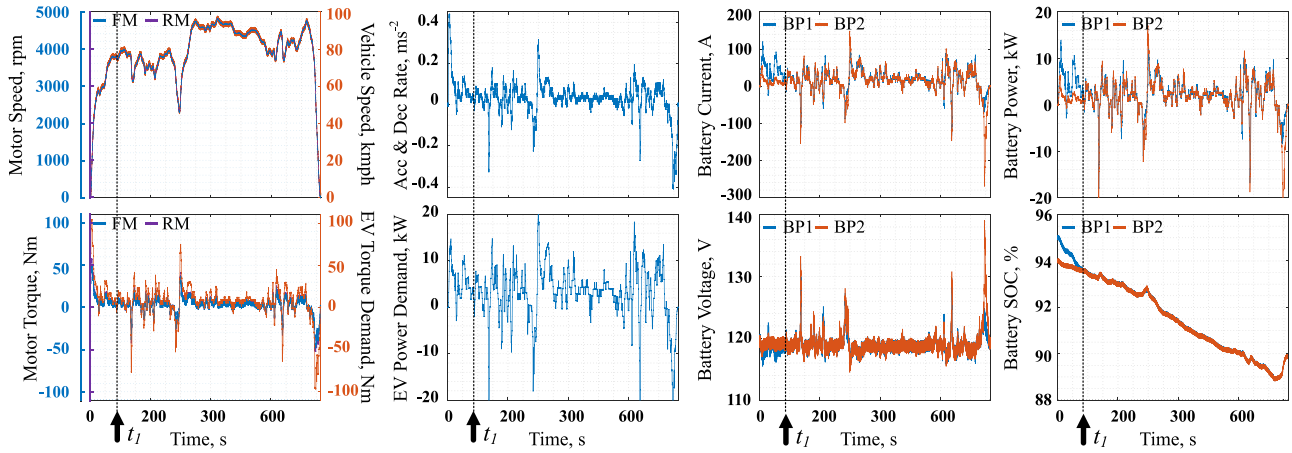

Fig. 8. Simulation results of the dual-motor D4WD EV with SoC balancing for the HFET driving cycle.

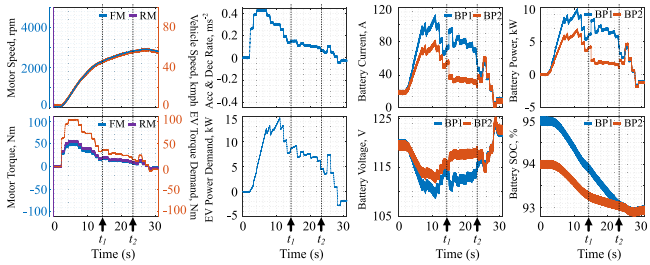

Fig. 9. Simulation results: SoC balance enabled at $t = t_1$ s during acceleration.

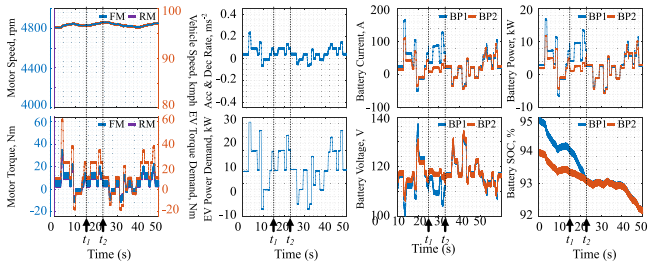

Fig. 10. Simulation results: SoC balance enabled at $t = t_1$ s during running.

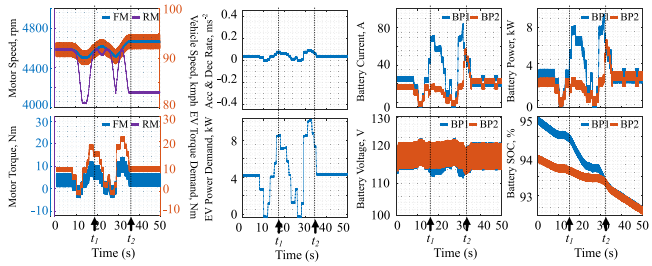

Fig. 11. Simulation results: SoC balance enabled at $t = t_1$ s during turning.

Fig. 12. Simulation results: SoC balance enabled at $t = t_1$ s during regenerative braking.

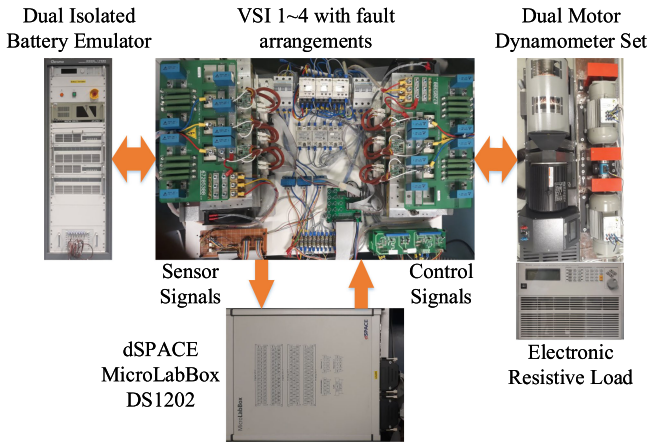

Fig. 13. Experimental hardware prototype of the dual-motor D4WD EV.

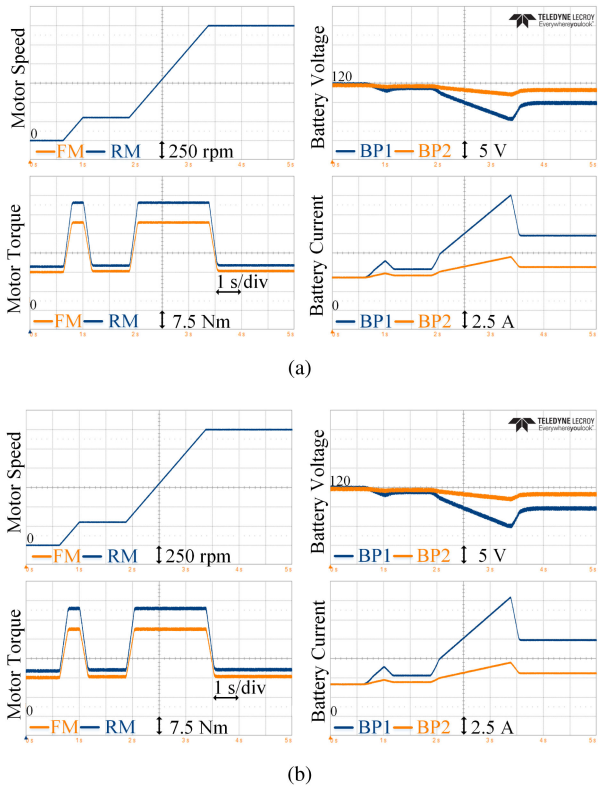

Fig. 14. Torque and current ripple performance analysis for (a) the proposed MPDTC and (b) MPC [7].

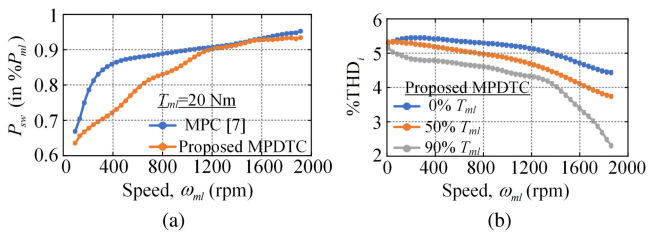

Fig. 15. Experimental results. Plot of (a) VSI switching losses and (b) %THD$_i$ with respect to ω_{ml} at various load conditions.

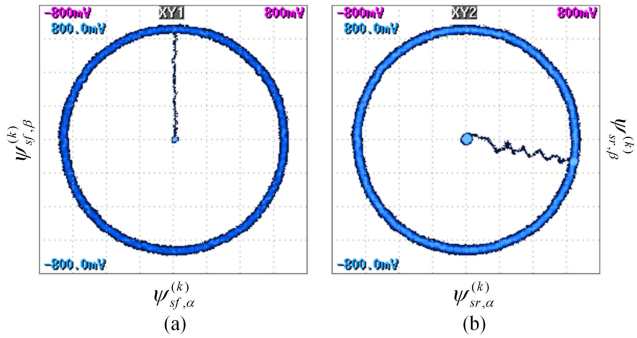

Fig. 16. Experimental results. Plot of stator flux $\psi_{sf}^{(k)}$ in the $\alpha\beta$ plane for (a) FM and (b) RM with a wide range of speed variations.

TABLE II
EXPERIMENTAL PARAMETERS OF THE DUAL-MOTOR D4WD EV

OEWIM Experimental Parameters
3Φ, 415 V, 5 kW, 10.5 A, 60 Hz, 1740 rpm, 0.87 PF
R_s =0.8593 Ω, R_r =1.033 Ω, $L_{ls} = L_{lr} = 6.8$ mH
l_m =170.2 mH, $J = 0.038$ kgm^2, $B = 0.001$
Experimental VSI Specifications
V_{dc}=600 V, $V_{ac,L-L}$=467 V, I_{ac}=50 A
P_{ac}=35 kW, P_{loss}=0.01P_{ac}, f_{sw}=30 kHz, cos ϕ=0.87
Battery Emulator Specifications
120 V, 100 A, 10 kW, Eff.>90%, PF>0.95, THD$_i$ <5%

TABLE III
RIPPLE % COMPARISON FOR REAR OEWIM (RM) WITH THE PROPOSED MPDTC AND MPC [7] AT THE SPEED OF 300 AND 1500 R/MIN

Parameters (in %)	Proposed MPDTC		MPC [7]		% Improvement	
	300 rpm	1500 rpm	300 rpm	1500 rpm	300 rpm	1500 rpm
ΔT_{ml}	2.9	3.3	6.7	7.4	56.7	55.4
$\Delta\omega_{ml}$	2.9	7.5	4.3	12.4	32.5	39.5
ΔP_{sl}	1.2	2.5	2.9	9.8	58.6	74.4
ΔI_{sl}	2.4	5.1	6.5	8.1	63.07	37.03
ΔI_{BP1}	8.9	11.8	10.9	13.8	18.3	14.4
ΔI_{BP2}	7.82	10.95	9.89	12.72	20.93	13.91

proposed controller works in such a way that BP2 is charged quicker than BP1, and the SoCs of both BPs are balanced at $t = t_2$ s.

B. Hardware Results

The proposed method has been evaluated experimentally using the experimental test prototype shown in Fig. 13. It consists of four VSIs, dSPACE MicroLabBox DS1202 platform, two isolated battery emulators, and dual OEWIM with dynamo meter set. The isolated battery emulator is controlled through the dSPACE platform. The experimental setup and controller parameters are listed in Table II. In order to test the performance of the proposed MPDTC scheme, dual motor speed and torque along with the BP voltages and currents are shown in Fig. 14(a) and are compared with the performance of MPC [7] in Fig. 14(b). It is observed that the proposed MPDTC provides better dynamics with reduced torque and current ripple. This can also be verified from the experimentally measured ripple % quantified in Table III.

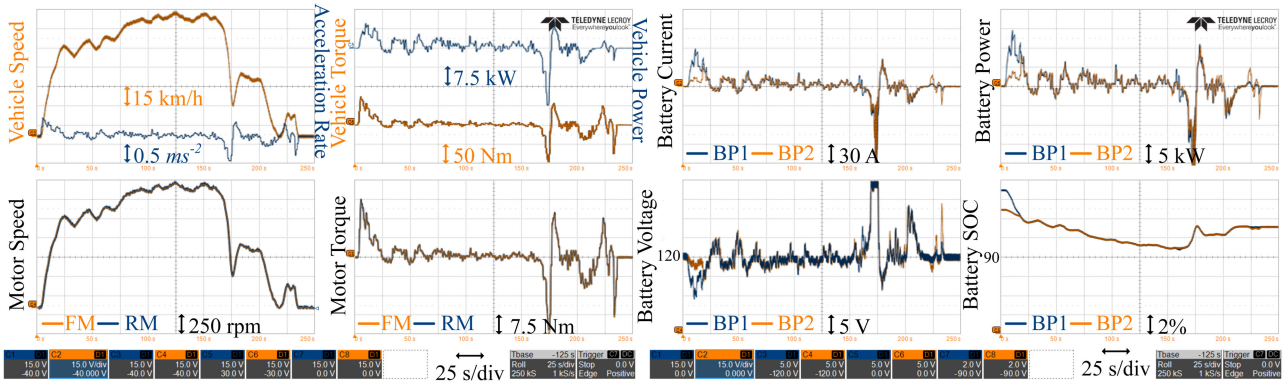

Fig. 17. Hardware results of the dual-motor D4WD EV with SoC balancing while using portion of FTP75 driving cycle.

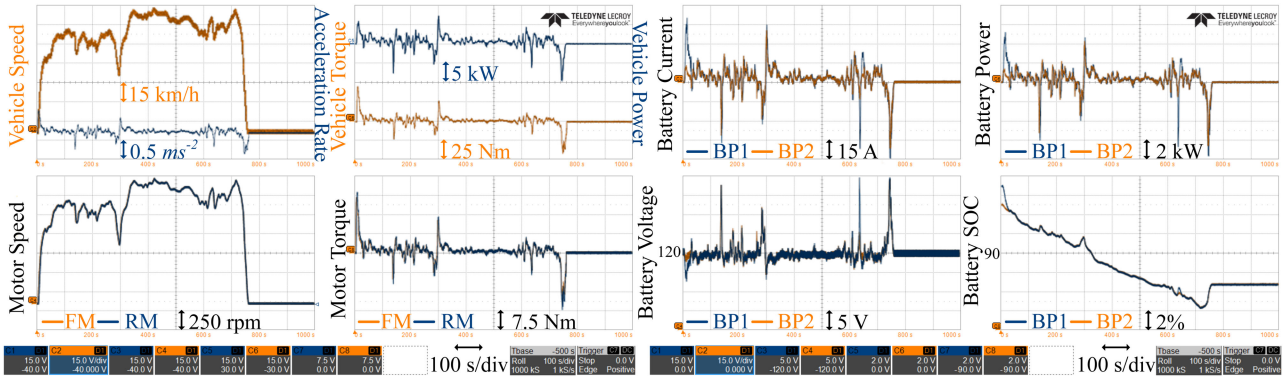

Fig. 18. Hardware results of dual motor D4WD EV with SoC balancing while using HFET driving cycle.

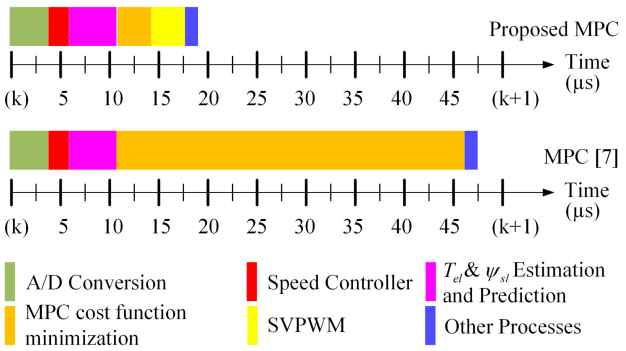

Fig. 19. Computational timing diagram of real-time implementation for the proposed MPDTC scheme and MPC [7].

Fig. 15(a) illustrates switching loss corresponding to speed variation for the proposed MPDTC and MPC [7]. It is observed that the switching losses are more prominent for MPC [7] as compared to the proposed MPDTC, whereas the switching losses for both the methods are almost equal near the nominal speed of the motors. The % current THD (%THD$_i$) verses speed variation is demonstrated in Fig. 15(b) for both the motors at different loading conditions. The stator currents have lower %THD$_i$ at higher speed with 90% of T_{ml}, while %THD$_i$ is higher at no load condition. The stator flux trajectory in the $\alpha\beta$-axis is provided in Fig. 16 for both the motors in order to show the effectiveness of the proposed MPDTC. It is observed that both the motor drives are able to maintain its stator flux to its nominal value of 0.687 Wb.

The SoCs of BP1 and BP2 are kept at 96% and 95%, respectively. For each driving cycle assessment, the same voltage level of the battery is considered in order to simplify the analysis. The tests have been carried out for the FTP75 and HFET driving cycles, and the performance is shown in Figs. 17 and 18, respectively. It can be observed that in both test cycles, initially, SoC balance is not enabled for $0 < t < t_1$ s, and by applying the proposed MPDTC controller, the initial differences in the SoC levels of both BPs are balanced at time $t = t_1$ s. These experimental results are in agreement with simulation results and also with the theoretical results and ensure SoC balance of both the BPs in all operating conditions of EV, such as acceleration, running, turning, and deceleration.

A comparison of timing information between the proposed dual-motor drive MPDTC scheme and MPC [7] is illustrated in Fig. 19. The microprocessor burden for the entire control process, involving analog-to-digital (A/D) conversion, speed control, T_{el}, ψ_{sl} estimation and prediction, cost function minimization, and switching pulse generation, which is imposed by the proposed MPDTC and MPC [7] in real time implementation, is evaluated. The other processes for both the schemes in Fig. 19 include nonideal delay corrections, input–output interface configuration, interrupt control, and pulsewidth modulation synchronization. It can be noticed that the cost function minimization process for MPC [7] requires approximately 35 μs, while

the proposed MPDTC needs 3.5 μs; as stated earlier, a reduction of 80–90% computational burden is achieved. Additionally, the implementation of SVPWM includes a further 3.5 μs in order to produce switching pulse at a constant switching frequency. In the case of the proposed MPDTC, the overall computational time of 7 μs is involved in both cost minimization and switching pulse generation, which is 1/5 times that of the MPC [7]. The proposed MPDTC exhibits a significant advantage over the MPC [7] approach for a wide range of speed variations, where switching frequencies (up to 20 kHz) are utilized.

IV. Conclusion

In this article, a modified two-stage MPC with SoC balancing dual-OEWIM-based D4WD was proposed, where the speed and torque control of the OEWIM with SoC balance were achieved. The two-stage optimization was adopted to minimize the effect of weight factor tuning, which facilitates fast computation. The effectiveness of the proposed SoC balancing was studied through simulation and verified through hardware experimental tests for different driving conditions. Also, the proposed drive was verified through simulation as well as hardware experiments for HFET and portion of FTP75 test driving cycle. The proposed MPDTC dual-OEWIM-based D4WD will find applications in high-power EVs. Combining the above algorithm with the FTO under inverter fault is a challenging research work for the future.

References

[1] X. Wang, Z. Wang, Z. Xu, M. Cheng, W. Wang, and Y. Hu, "Comprehensive diagnosis and tolerance strategies for electrical faults and sensor faults in dual three-phase PMSM drives," *IEEE Trans. Power Electron.*, vol. 34, no. 7, pp. 6669–6684, Jul. 2019.

[2] Y. Fan, R. Cui, and A. Zhang, "Torque ripple minimization for inter-turn short-circuit fault based on open-winding five phase FTFSCW-IPM motor for electric vehicle application," *IEEE Trans. Veh. Technol.*, vol. 69, no. 1, pp. 282–292, Jan. 2020.

[3] A. Salem and M. Narimani, "A review on multiphase drives for automotive traction applications," *IEEE Trans. Transp. Electrific.*, vol. 5, no. 4, pp. 1329–1348, Dec. 2019.

[4] G. Pellegrino, A. Vagati, B. Boazzo, and P. Guglielmi, "Comparison of induction and PM synchronous motor drives for EV application including design examples," *IEEE Trans. Ind. Appl.*, vol. 48, no. 6, pp. 2322–2332, Nov. 2012.

[5] J. de Santiago *et al.*, "Electrical motor drivelines in commercial all-electric vehicles: A review," *IEEE Trans. Veh. Technol.*, vol. 61, no. 2, pp. 475–484, Feb. 2012.

[6] D. Ronanki and S. S. Williamson, "A simplified space vector pulse width modulation implementation in modular multilevel converters for electric ship propulsion systems," *IEEE Trans. Transp. Electrific.*, vol. 5, no. 1, pp. 335–342, Mar. 2019.

[7] R. E. Kodumur Meesala, V. P. K. Kunisetti, and V. K. Thippiripati, "Enhanced predictive torque control for open end winding induction motor drive without weighting factor assignment," *IEEE Trans. Power Electron.*, vol. 34, no. 1, pp. 503–513, Jan. 2019.

[8] S. Lakhimsetty, V. S. P. Satelli, R. S. Rathore, and V. T. Somasekhar, "Multilevel torque hysteresis-band based direct-torque control strategy for a three-level open-end winding induction motor drive for electric vehicle applications," *IEEE Trans. Emerg. Sel. Topics Power Electron.*, vol. 7, no. 3, pp. 1969–1981, Sep. 2019.

[9] S. Srinivas and K. R. Sekhar, "Theoretical and experimental analysis for current in a dual-inverter-fed open-end winding induction motor drive with reduced switching PWM," *IEEE Trans. Ind. Electron.*, vol. 60, no. 10, pp. 4318–4328, Oct. 2013.

[10] W. Hu, H. Nian, and D. Sun, "Zero-sequence current suppression strategy with reduced switching frequency for open-end winding PMSM drives with common DC BUS," *IEEE Trans. Ind. Electron.*, vol. 66, no. 10, pp. 7613–7623, Oct. 2019.

[11] X. Hu, Y. Li, C. Lv, and Y. Liu, "Optimal energy management and sizing of a dual motor-driven electric powertrain," *IEEE Trans. Power Electron.*, vol. 34, no. 8, pp. 7489–7501, Aug. 2019.

[12] S. Yang, X. Sun, M. Ma, X. Zhang, and L. Chang, "Fault detection and identification scheme for dual-inverter fed OEWIM drive," *IEEE Trans. Ind. Electron.*, vol. 67, no. 7, pp. 6112–6123, Jul. 2020.

[13] X. Yuan and J. Wang, "Torque distribution strategy for a front- and rear-wheel-driven electric vehicle," *IEEE Trans. Veh. Technol.*, vol. 61, no. 8, pp. 3365–3374, Oct. 2012.

[14] N. Mutoh, "Driving and braking torque distribution methods for front- and rear-wheel-independent drive-type electric vehicles on roads with low friction coefficient," *IEEE Trans. Ind. Electron.*, vol. 59, no. 10, pp. 3919–3933, Oct. 2012.

[15] L. Hsu and T. Chen, "An optimal wheel torque distribution controller for automated vehicle trajectory following," *IEEE Trans. Veh. Technol.*, vol. 62, no. 6, pp. 2430–2440, Jul. 2013.

[16] U. R. Muduli, A. R. Beig, K. A. Jaafari, J. Y. Alsawalhi, and R. K. Behera, "Interrupt-free operation of dual-motor four-wheel drive electric vehicle under inverter failure," *IEEE Trans. Transp. Electrific.*, vol. 7, no. 1, pp. 329–338, Mar. 2021.

[17] W. Hu, H. Nian, and T. Zheng, "Torque ripple suppression method with reduced switching frequency for open-winding PMSM drives with common DC bus," *IEEE Trans. Ind. Electron.*, vol. 66, no. 1, pp. 674–684, Jan. 2019.

[18] M. A. Masadeh, K. S. Amitkumar, and P. Pillay, "Power electronic converter-based induction motor emulator including main and leakage flux saturation," *IEEE Trans. Transp. Electrific.*, vol. 4, no. 2, pp. 483–493, Jun. 2018.

[19] S. Busquets-Monge *et al.*, "Multibattery fed neutral-point-clamped DC-AC converter with SoC balancing control to maximize capacity utilization," *IEEE Trans. Ind. Electron.*, vol. 67, no. 1, pp. 16–27, Jan. 2020.

[20] J. Oncken and B. Chen, "Real-time model predictive powertrain control for a connected plug-in hybrid electric vehicle," *IEEE Trans. Veh. Technol.*, vol. 69, no. 8, pp. 8420–8432, Aug. 2020.

[21] X. Zeng and J. Wang, "A parallel hybrid electric vehicle energy management strategy using stochastic model predictive control with road grade preview," *IEEE Trans. Control Syst. Technol.*, vol. 23, no. 6, pp. 2416–2423, Nov. 2015.

[22] H. Borhan, A. Vahidi, A. M. Phillips, M. L. Kuang, I. V. Kolmanovsky, and S. Di Cairano, "MPC-based energy management of a power-split hybrid electric vehicle," *IEEE Trans. Control Syst. Technol.*, vol. 20, no. 3, pp. 593–603, May 2012.

[23] S. D. Cairano, D. Bernardini, A. Bemporad, and I. V. Kolmanovsky, "Stochastic MPC with learning for driver-predictive vehicle control and its application to HEV energy management," *IEEE Trans. Control Syst. Technol.*, vol. 22, no. 3, pp. 1018–1031, May 2014.

[24] T. Dragicevic and M. Novak, "Weighting factor design in model predictive control of power electronic converters: An artificial neural network approach," *IEEE Trans. Ind. Electron.*, vol. 66, no. 11, pp. 8870–8880, Nov. 2019.

[25] F. Wang, H. Xie, Q. Chen, S. A. Davari, J. Rodriguez, and R. Kennel, "Parallel predictive torque control for induction machines without weighting factors," *IEEE Trans. Power Electron.*, vol. 35, no. 2, pp. 1779–1788, Feb. 2020.

[26] T. Liu, A. Chen, C. Qin, J. Chen, and X. Li, "Double vector model predictive control to reduce common-mode voltage without weighting factors for three-level inverters," *IEEE Trans. Ind. Electron.*, vol. 67, no. 10, pp. 8980–8990, Oct. 2020.

[27] L. Zhang, Y. Fan, R. D. Lorenz, A. Nied, and M. Cheng, "Design and comparison of three-phase and five-phase FTFSCW-IPM motor open-end winding drive systems for electric vehicles applications," *IEEE Trans. Veh. Technol.*, vol. 67, no. 1, pp. 385–396, Jan. 2018.

[28] X. Lu, K. Sun, J. M. Guerrero, J. C. Vasquez, and L. Huang, "State-of-charge balance using adaptive droop control for distributed energy storage systems in dc microgrid applications," *IEEE Trans. Ind. Electron.*, vol. 61, no. 6, pp. 2804–2815, Jun. 2014.

[29] M. J. Akhtar and R. K. Behera, "Space vector modulation for distributed inverter-fed induction motor drive for electric vehicle application," *IEEE Trans. Emerg. Sel. Topics Power Electron.*, vol. 9, no. 1, pp. 379–389, Feb. 2021.

[30] R. Wang and J. Wang, "Fault-tolerant control with active fault diagnosis for four-wheel independently driven electric ground vehicles," *IEEE Trans. Veh. Technol.*, vol. 60, no. 9, pp. 4276–4287, Nov. 2011.

Utkal Ranjan Muduli (Member, IEEE) received the B.Tech. degree in electrical and electronics engineering from the Biju Patnaik University of Technology Odisha, Rourkela, India, in 2011, and the M.Tech. degree in electrical engineering from the Indian Institute of Technology Gandhinagar, Gandhinagar, India, in 2014. He is currently working toward the Ph.D. degree in electrical engineering with the Indian Institute of Technology Patna, Patna, India.

In 2019, he was a Visiting Researcher with the Department of Electrical Engineering and Computer Science, Khalifa University, UAE, where he is currently working as a Research Associate. His research interests include modulation strategies for multiphase motor drives, matrix converters and its control, battery power management, and wireless power transfer.

Abdul R. Beig (Senior Member, IEEE) received the B.Eng. degree in electrical and electronics engineering from the National Institute of Technology Karnataka, Surathkal, India, in 1989, and the M.Tech. and Ph.D. degrees in electrical engineering from the Indian Institute of Science, Bengaluru, India, in 1998 and 2004, respectively.

He is currently an Associate Professor with the Advanced Power and Energy Center (APEC), Department of Electrical Engineering and Computer Science, Khalifa University of Science and Technology, Abu Dhabi, UAE. He is currently leading the research theme on transportation electrification under APEC. His current research include electric vehicle drive train, high-gain converters, autotuning of grid-connected converters, modular multilevel converters, and SiC-based converters.

Dr. Beig is an Associate Editor for the IEEE TRANSACTIONS ON INDUSTRY APPLICATIONS.

Ranjan Kumar Behera (Senior Member, IEEE) received the B.Eng. degree in electrical engineering from the Regional Engineering College (now National Institute of Technology) Rourkela, Rourkela, India, in 1998, and the M.Tech. and Ph.D. degrees in electrical engineering from the Indian Institute of Technology, Kanpur, India, in 2003 and 2009, respectively.

He was a Visiting Scholar with the Energy Systems Research Center, Tennessee Technological University, Cookeville, TN, USA, in 2008. Since 2009, he has been a Faculty Member and is currently an Associate Professor with the Department of Electrical Engineering, Indian Institute of Technology, Patna, India. His research interests include nonlinear control theory application to power electronic converters, pulsewidth modulation techniques, and multiphase electric drive control.

Khaled Al Jaafari (Senior Member, IEEE) received the B.Sc. and M.Sc. degrees in electrical engineering from the Petroleum Institute, Abu Dhabi, UAE, in 2006 and 2011, respectively, and the Ph.D. degrees in electrical and computer engineering from Texas A&M University, College Station, TX, USA, in 2016.

He is currently an Assistant Professor with the Khalifa University of Science and Technology, Abu Dhabi. His research interests include machine condition monitoring, power system analysis, power system protection, and power quality studies.

Jamal Y. Alsawalhi (Member, IEEE) received the B.S., M.S., and Ph.D. degrees in electrical engineering from Purdue University, West Lafayette, IN, USA, in 2009, 2011, and 2014, respectively.

He is currently an Assistant Professor of electrical engineering with Khalifa University of Science and Technology, Abu Dhabi, UAE. His research interests include electrical machine design and analysis for transportation electrification application.